Innovative method of ODS steels manufacturing by direct introduction of pyrochlore phase through milling

E. Simondon, P. -F. Giroux, J. Ribis, G. Spartacus, L. Chaffron, T. Gloriant

Title

« Innovative method of ODS steels manufacturing by direct introduction of pyrochlore phase through milling »

Authors

E. Simondon[1], P.-F. Giroux[1], J. Ribis[1], G. Spartacus[1], L. Chaffron[1], Th. Gloriant[2]

[1] Université Paris-Saclay, CEA, Service de Recherches Métallurgiques Appliquées, 91191, Gif-sur-Yvette, France
[2] Univ Rennes, INSA Rennes, CNRS, ISCR – UMR 6226, F-35000 Rennes, France

Abstract

This study concerns the development of an innovative manufacturing process for oxide-dispersion strengthened steels (hereafter referred to as "ODS") by mechanosynthesis. As part of materials development for Sodium-cooled Fast Reactors (SFR), the aim is to prevent the growth of undesirable micrometric precipitates which can drastically degrade steel's mechanical properties. This new process introduces $Y_2Ti_2O_7$ pyrochlore oxide nanoparticles directly into Fe-Cr metallic powder through mechanical milling, as compared to the standard Y_2O_3 + TiO_2. This study enables the validation of the method of introducing precipitates in the form of $Y_2Ti_2O_7$ oxides as an efficient way to obtain competitive ODS steels, with a more homogeneous microstructure, less coarse precipitates and more reliable impact properties compared to the conventional process. Moreover, it reveals the importance of the features of the manufacturing process, particularly of milling intensity and reinforcement rate, on the microstructure and mechanical properties of ODS steel. The results reveal promising perspectives concerning the features of ODS steel manufacturing.

Keywords

ODS steel, oxide-dispersion strengthened, mechanical milling, mecanosynthesis, powder metallurgy, pyrochlore oxide $Y_2Ti_2O_7$, nanostructure, microstructure, mechanical properties

1. Introduction

In order to address the rising global demand in energy, the diminution of fossil resources and to tackle the rise of greenhouse gases production, nuclear power represents a promising solution. The long-term development of future fission (Gen IV) and fusion power plants is of major interest. Indeed, Gen IV power plants are characterized by an optimization and major improvements in terms of safety, cost-effectiveness, use of natural uranium resources and radioactive waste management, compared to the current power plants. The industrial development of thermonuclear fusion technology, in the longer term, will provide a strong solution in all these areas.

These new technologies have common needs of core material properties: high temperature mechanical strength, swelling resistance under irradiation and tenacity before and after irradiation. Currently, the performances of steels available on an industrial scale are not optimal.

Oxide Dispersion Strengthened (ODS) steels are the main candidates able to meet the specifications of the materials of fuel cladding for future Sodium-Cooled Fast Reactor (SFR).

They consist of a ferritic-martensitic matrix whose BCC structure induces very little swelling under irradiation [1]. In addition, this matrix is reinforced by a homogeneous distribution of nano-sized precipitates of Y-Ti-O oxides. These precipitates have the role, on the one hand, of slowing the movement of dislocations in order to increase mechanical strength at high temperature [2]–[4], and on the other hand, of trapping irradiation defects [5], [6]. These materials therefore combine the advantage of good dimensional stability under irradiation and good creep resistance at high temperature.

ODS steels are produced by a complex process of powder metallurgy. Nanometric powders Y_2O_3 and TiO_2 (or TiH_2) are milled together with a metallic powder by mechanical alloying (MA). Under the action of repeated shocks, the reinforcing elements are finely dispersed in the metallic matrix. The subsequent powder densification treatment then leads to the germination of nanoprecipitates, mainly of composition $Y_2Ti_2O_7$ [7]. However, in addition to the nanometric precipitation, these materials contain a population of micrometric precipitates of various compositions, in particular chromium carbides and titanium oxides. The presence of large chromium carbides of type $M_{23}C_6$ (M=Fe,Cr,W) located mostly along grain boundaries [8]–[13], is the result of a carbon contamination during the milling process [12]–[15]. Large titanium oxides (> 50 nm) of composition TiO_2 have also been referenced many times in the literature [10], [14], [16]–[19]. These particles form 'chaplets' along prior particle boundaries, which correspond to the surface of milled powder particles before compaction [20]. An overstated Ti content in the matrix promotes the formation of these micrometric phases [21], [22]. These large precipitates of various chemical compositions are undesirable and lead to a drastic decrease in mechanical properties [23]–[25].

For this reason, a new method of ODS steel manufacturing is proposed to avoid the presence of undesirable micrometric precipitates. This innovative process is based on the direct introduction of stable phase $Y_2Ti_2O_7$ as reinforcement element in the metallic matrix, instead of the powders Y_2O_3 and TiH_2 usually used. The aim is to avoid the germination step of the precipitates with different size and chemical composition. A similar process was implemented by Liu *et al.* in the development of aluminum-reinforced ODS steels to prevent the appearance of Al-Ti-O oxides [26]. The purpose of this work is therefore to investigate the feasibility of producing ODS steels by this new method. The role of milling intensity and oxide addition is also examined.

2. Materials and Methods/Experimental

a. Material preparation

For synthesizing the ODS steel, a ferritic pre-alloyed Fe-14Cr-1W wt.% powder (Nanoval) is milled together with a pyrochlore $Y_2Ti_2O_7$ nanostructured powder. Before the milling, the metallic FeCrW powder is degassed at 400°C for 24 h under secondary vacuum (10^{-6} bar) in a rotational oven. The pyrochlore powder is synthesized by mechanical milling method developed in earlier works [27].

Both ferritic Fe-14Cr-1W and pyrochlore powders are then loaded in the vial, with proportions chosen to lead to a final alloy with 0.5 wt.% of $Y_2Ti_2O_7$. The loading is carried in an argon-flushed glove-box and the vial is sealed to avoid oxygen contamination. The milling experiments is conducted in a ZOZ CM-01 mill for a duration of 20 hours, with 200 g of powder and 2 kg of 100C6 grade steel balls, under a dynamic helium flux. After the milling, the powder is collected in a container without any contact to ambient air to prevent contamination (the procedure makes sure the powder is not in contact with air at any point of

the process, starting from the first thermal treatment). The milled powder is introduced in a can before degassing for 24 h at 130°C under secondary vacuum. In a previous study carried out on the $Y_2Ti_2O_7$ oxide [27], we observed that the as-milled powder presents a mostly amorphous structure. After heat treatment of the milled powder and according to our DTA an synchrotron analyses, crystallization into a fluorite-like structure occurs first at around 800 °C followed by the transformation into of the stable pyrochlore structure at around 900 °C. It is therefore necessary to choose a high temperature for the consolidation (at least > to 900°C). The consolidation was then performed by hot extrusion of the can at 1100°C to ensure the presence of the stable pyrochlore structure in the consolidated materials..

For comparison purposes, different milling intensities are used, arbitrarily denominated I1, I2 I3 and I4 with rising rotational speed, and hence rising intensity (I3 is used for the reference material). Two additional grades are also prepared with different $Y_2Ti_2O_7$ contents (0.0 and 0.25 wt.%). Finally, to evaluate the benefit of introducing the ODS particles via $Y_2Ti_2O_7$ powder, a "conventional ODS" is prepared. The same process as for the reference material is used, except for the added oxide powder: instead of $Y_2Ti_2O_7$, a stoichiometric mix of Y_2O_3 and TiO_2 nanometric powders (Y_2O_3:2TiO_2) is used. The different processing conditions are summarized in Table 1.

Sample denomination	0.5P-I1	0.5P-I2	0.5P-I3	0.5P-I4	0-I3	0.25P-I3	0.5CV-I3
Milling intensity	I1	I2	I3	I4	I3	I3	I3
Quantity of oxide	0.50 wt. %	0.50 wt. %	0.50 wt. %	0.50 wt. %	0.00 wt. %	0.25 wt. %	0.50 wt. %
Type of oxide addition	$Y_2Ti_2O_7$: Pyrochlore (P)	$Y_2Ti_2O_7$: Pyrochlore (P)	$Y_2Ti_2O_7$: Pyrochlore (P)	$Y_2Ti_2O_7$: Pyrochlore (P)	-	$Y_2Ti_2O_7$: Pyrochlore (P)	Y_2O_3 + TiO_2 : Conventional (CV)

Table 1 : Summary of the processing parameters

b. Characterizations

Scanning Electron Microscopy (SEM) observations were carried out on a HIROX SH-3500MB microscope working at 20 kV. For each sample, the mean diameter and surface fraction of the larger inclusions were estimated by image analysis from the SEM micrographs. The measurements take into account objects from 0.1 to 1 µm. The Transmission Electron Microscopy (TEM) observations were performed using a JEOL 2100 operating at 200 kV equipped with a Gatan Imaging Filter (GIF) for Energy Filtered TEM (EFTEM). The precipitates distribution data are measured on bright field images with software Digital micrograph. A JEOL 2010 working at 20 kV was used for the High Resolution (HR) TEM. The thin foils were punched out in bulk specimen and mechanically thinned and electropolished.

SAXS measurements were performed at the ESRF (European Synchrotron Radiation Facility) at the BM02-D2AM beamline on foils of thickness smaller than 70 µm. The X-ray (16.829 keV) scattering pattern was detected using a 2D PILATUS detector with a detector-to-sample distance of around 0.8 m. 2D scattering patterns were then azimuthally integrated, corrected from background noise and normalized by incident beam flux, specimen thickness and solid angle. Intensity where then reduced into absolute unit using glassy-C as a secondary standard. Mean radius and number density of precipitates were extracted using least square

fitting of a lognormal distribution of sphere model to the experimental data, with the assumption of $Y_2Ti_2O_7$ pyrochlore precipitates.

Vickers microhardness indentation tests were performed with a Leica VMHT 30A using 100 g load, 15 s dwell time, at room temperature. Tensile tests were carried out in air at room temperature, 400°C and 650°C on cylindrical specimens (TMAS23 494 02A) machined along the extrusion direction. Impact tests were performed by using mini-Charpy impact specimen (3mm×4mm×27 mm, V-notch 60° angle/1mm depth) machined along the extrusion direction. A tanh fit of the curve was applied to the data to determine the Ductile-to-Brittle Transition Temperature (DBTT) [28].

Oxygen-content was measured in milled powders via reductive fusion and infrared absorption with a chemical analyzer HORIBA EMGA-800. Three measurements were performed for each powder, with 300 mg samples.

3. Results and discussion

a. Influence of the introduction of $Y_2Ti_2O_7$ as reinforcement powder

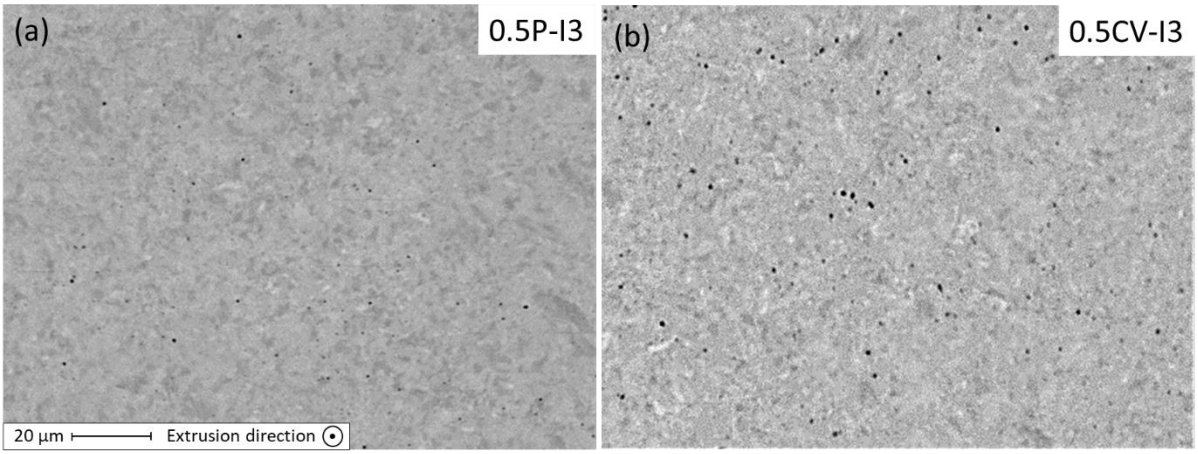

Figure 1: SEM micrographs (BSE) of samples (a) 0.5P-I3 and (b) 0.5CV-I3

In order to determine the benefit of the innovative reinforcement method introduced by this study, microstructures and mechanical performances of samples produced with $Y_2Ti_2O_7$ addition (*0.5P-I3*) and Y_2O_3+TiO_2 addition (*0.5CV-I3*) are compared. Figure 1 shows SEM micrographs of the materials, revealing inclusions of about a few hundreds of nanometers. These inclusions represent a fraction surface of 0.67% for the conventional material *(0.5CV-I3*) against 0.33% for the material reinforced with pyrochlores oxides (*0.5P-I3*). Moreover, concerning precipitates, no segregation is observed at grain boundaries.

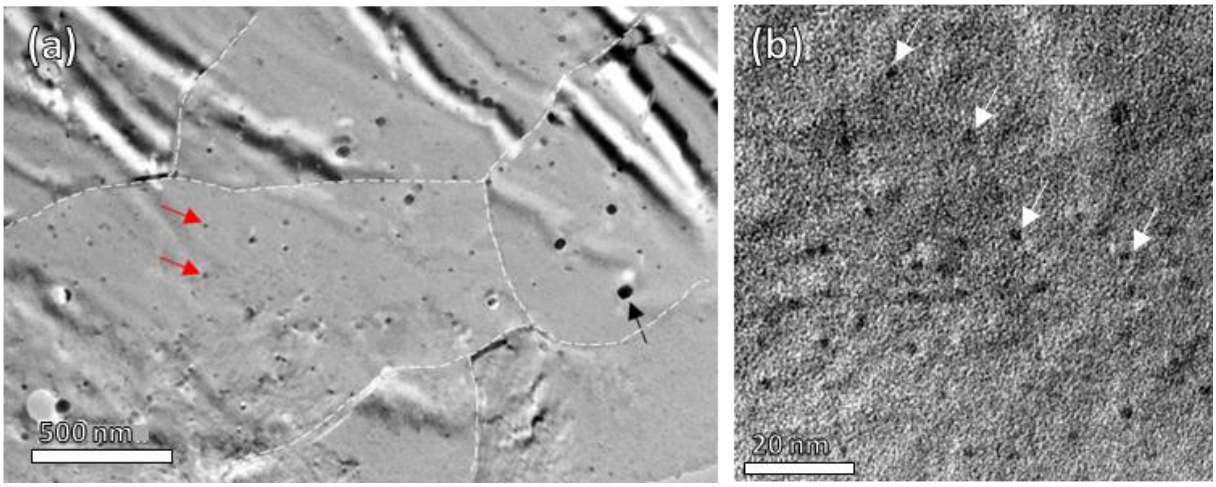

Figure 2: (a) Bright field TEM images of the microstructure of the 0.5P-I3 sample with different magnifications, grain boundaries are highlighted with dotted lines, (b) detailed view of the nano-oxide dispersion.

The microstructure of the materials is investigated by TEM observations (Figure 2). The bright field images reveal the existence of a nanosized distribution of precipitates in the matrix. At this scale, their distribution appears to be homogeneous within the grains. In particular, there is no observable segregation at grain boundaries (Figure 2.a). Observations performed with higher magnification micrograph (Figure 2.b) confirm the presence of inclusions with a size down to 2 nm. This attests to the feasibility to obtain steel with a homogeneous distribution of nanoparticles via the introduction of $Y_2Ti_2O_7$ as reinforcement.

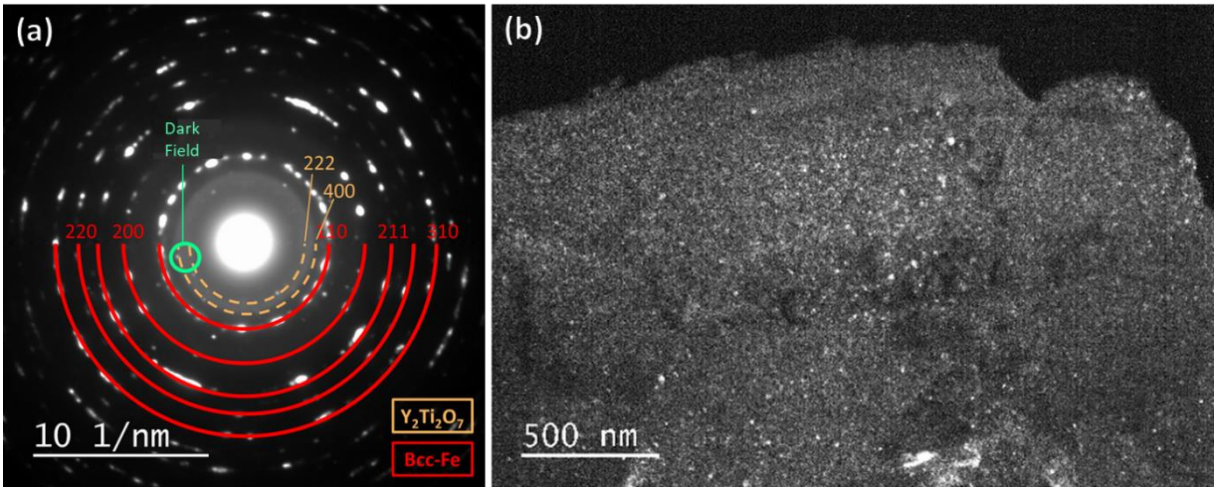

Figure 3 : (a) diffraction pattern of the ODS microstructure and (b) associated dark-field on the (400) spot of the pyrochlore structure, enlightening the distribution of nanoparticles in the matrix

Figure 3.a shows a diffraction pattern of sample *0.5-I4*. Its circular character is due to the small grain size of the ferritic matrix, involving a high number of grains diffracting in random orientations. In addition to the ferritic reflexions, referenced in red, a halo is observable on the diffraction pattern. In the same diameter range, spots corresponding to (400) and (222) reflexions of the $Y_2Ti_2O_7$ pyrochlore structure are identified. In Figure 3.b, the corresponding dark field image to a (400) spot brightens up a distribution of nanoparticles, which is another proof of their homogeneous repartition within the matrix. These observations

show that the structure of the nanoparticles is consistent with the $Y_2Ti_2O_7$ pyrochlore structure.

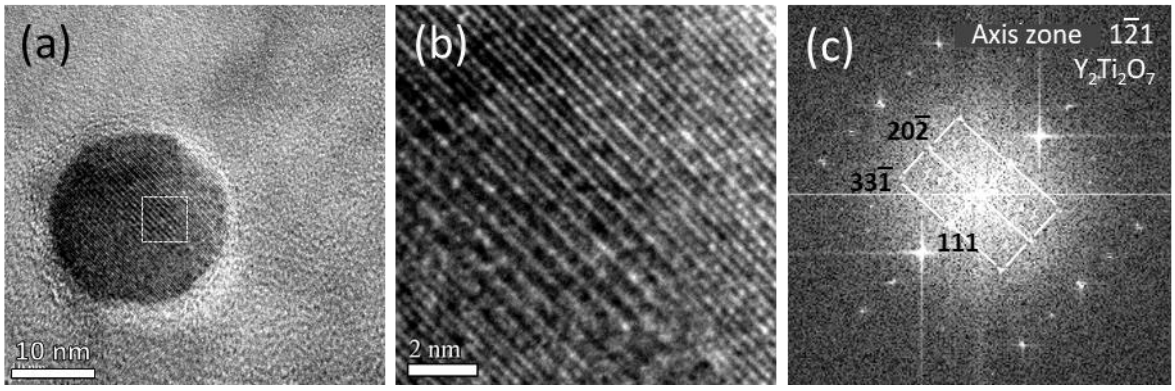

(d)

hkl	***Measured D_{hkl}***	***Theoretical D_{hkl} of $Y_2Ti_2O_7$***
202	3,54 Å	3,57 Å
331	3,07 Å	3,04 Å
111	5,67 Å	5,83 Å

Figure 4 : Precipitate from sample 0,25P-I3 ,(a) HRTEM image (b) zoom on the framed area (c) affiliated FFT, and (d) table summarizing the main measured interplanar distances and matching theoretical interplanar distances of the pyrochlore structure

High-Resolution Transmission Electron Microscopy (HRTEM) characterization are performed on the materials. An example of an analyzed particle of 21 nm diameter is presented in Figure 4.a. as well as an HR image of the framed area (Figure 4.b). The affiliated FFT (Figure 4.c) matches a F.C.C. structure in a [1$\bar{2}$1] axis zone. The measured interplanar distances match the pyrochlore structure with a measured lattice parameter of 10.02 Å (Figure 4.d). Several particles, from 5 to 50 nm, were analyzed by HRTEM and found to match the pyrochlore structure. These results confirm the presence of the expected structure pyrochlore $Y_2Ti_2O_7$ as nanosized particles in the extruded material.

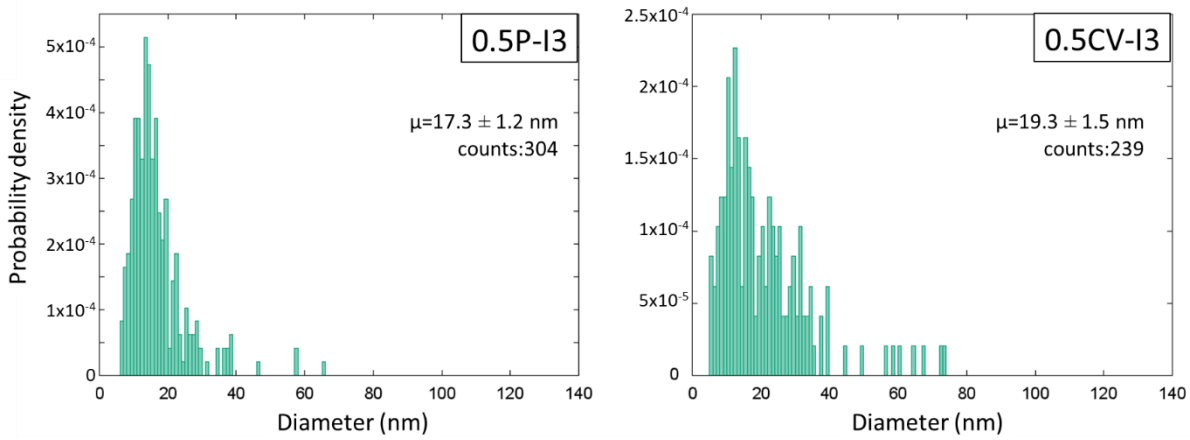

Figure 5 : Size distribution of precipitates measured by TEM image analysis

	TEM		***SAXS***	
	0.5P-I3	0.5CV-I3	0.5P-I3	0.5CV-I3

Mean diameter (nm)	17.30 ± 1.02	19.28 ± 1.54	2.4	2.6
Density (m^{-3})	6.73×10^{20}	5.29×10^{20}	2.30×10^{23}	1.20×10^{23}

Table 2: Mean diameter and density of particles measured in both materials by TEM and SAXS

Nanoprecipitates size distributions and densities are measured from the numerous bright field TEM images of the samples. The results are reported in Table 2Table 2: Mean diameter and density of particles measured in both materials by TEM and SAXS and the distribution histograms are shown in Figure 5. Only precipitates from 5 to 130 nm are taken into account, since smaller objects could not be resolved with the used magnification. The mean diameter of the measured particles is 17.3 nm for the pyrochlore-reinforced sample which is slightly lower than the mean diameter of the measured particles for the conventionally reinforced sample (19.3 mm). Figure 5 shows that the size distribution of the conventionally reinforced *0.5CV-I3* sample is broader towards larger diameters. Additionally, the density of particles is higher in the pyrochlore-reinforced sample (6.73×10^{20} m^{-3}) than in the conventionally reinforced sample (5.29×10^{20} m^{-3}) (Table 2). These results show that the introduction of reinforcement via $Y_2Ti_2O_7$ implies both a slight reduction of precipitates size, as well as a slight raise in their number density compared to their conventional introduction in the form $Y_2O_3 + TiO_2$.

Small Angle X-ray Scattering (SAXS) experiments are also used to obtain features of the smaller nano-precipitates population. This analytical method enables to characterize quantitatively in a larger volume the nanoparticles size distribution. The SAXS measurement campaign was performed at ESRF (Grenoble, France). Table 2 provides the mean diameter and number density of particles calculated from SAXS measurements, setting the lognormal dispersion at 0.2, with the assumption of $Y_2Ti_2O_7$ pyrochlore precipitates. The calculated mean diameters of precipitates from SAXS measurements are 2.4 nm for sample *0.5P-I3* and 2.6 nm for *0.5CV-I3* sample. These results are in the typical order of magnitude for ODS steel [29]–[31]. The precipitates number density of both samples are in the range of 10^{23} precipitates/m^3. This value is a slighlty smaller than the typical values for ODS steel found in the literature [29], [32], [33] .. 0.5P-I3 and 0.5CV-I3 samples both display a close density of nanoprecipitates.

Table 2 shows that the two measuring methods give different results. The precipitate density for both materials is three orders of magnitude higher with SAXS than with TEM. Indeed, the range of particle size reachable is different for the two methods. The used magnification for TEM imaging allows to measure objects from 5 nm, whereas calculations from SAXS measurements take into account the smaller nanoprecipitates. Both methods enable to conclude that the two materials present a high density of nanosized precipitates. In particular, the SAXS results, with a mean size of 2-3 nm and a nanoparticle density three orders of magnitude higher than with TEM analysis, show that a large number of very fine objects (smaller than 5 nm) are present in the material. Also, both methods show that the precipitation populations in both materials have features in the same order of magnitude.
It is worth noting that, according to our observations carried out by TEM and SAXS in the materials, no porosity could be detected. The consolidated materials are then fully dense.

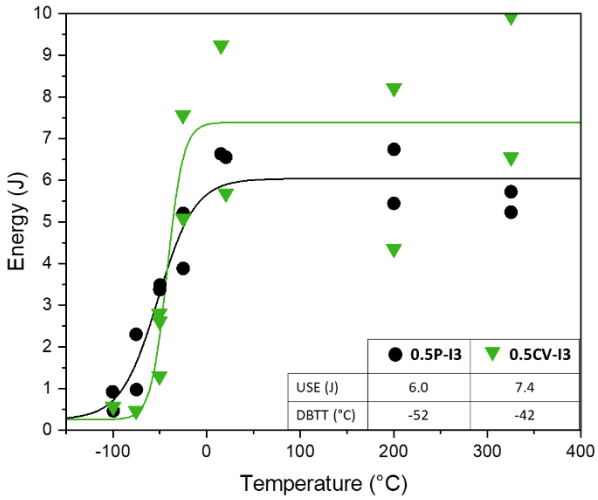

Figure 6 : Experimental data (points) and fitted-curves (lines) of impact tests performed on mini-Charpy specimen

Impact tests have been performed on mini-Charpy specimens machined from both materials. Figure 6 presents the experimental data (points) and the extrapolated energy curves. First, for both materials, the Upper Shelf Energy (USE) is higher than 6 J, and the DBTT is lower than -40°C. These results show that the features of produced material are comparable to the best results found in literature [8], [34]. Then, the comparison of both materials reveals that the USE of *0.5CV-I3* sample is higher than for *0.5P-I3* sample (7,4 J against 6,0 J) and its DBTT is higher (-42,1°C against -52,0 °C). Moreover, it is noticeable that *0.5P-I3* impact test results is characterized by a smaller dispersion than *0.5CV-I3*. This might be attributed to the better homogeneity of the material reinforced in $Y_2Ti_2O_7$ compared to the conventional material.

b. Influence of the milling intensity

In order to optimize the milling process, several milling intensities, arbitrarily denominated I1, I2, I3, I4 in the order of increasing intensity, are tested. Figure 7 shows a TEM bright field image of sample 0.5P-I2, where agglomerates of particles can be identified (circled in red). Such agglomerates are observed in both samples of lower intensity (0.5P-I1 and 0.5P-I2), whereas no such observations could be made on the samples with higher milling intensity (0.5P-I3 and 0.5P-I4). Thus, the presence of agglomerates could be attributed to a less efficient milling that would not distribute the introduced $Y_2Ti_2O_7$ particles in a homogeneous way.

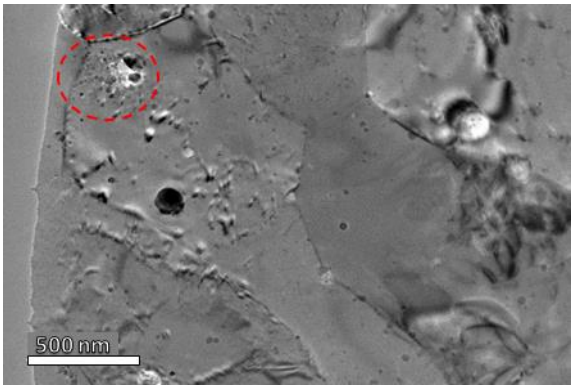

Figure 7: TEM bright field of sample 0.5P-I2 showing a cluster of particles due to an insufficient milling

The consolidated materials are characterized by low magnification bright field TEM to evaluate the grain size (Figure 8). The software ImageJ is used to determine from the presented images the mean size and anisotropy factor of the grains (Table 3). For all samples, the mean anisotropy factor is of 1.5, and no preferential orientation is found in this plan (transversal cut). These results are consistent with commonly reported observations in literature [21].

The rods elaborated with different milling intensities display mean grain sizes of 1,23 ± 0,13 µm (0.5P-I1), 0,79 ± 0,07 µm (0.5P-I2), 0,67 ± 0,07 (0.5P-I3) and 0,33 ± 0,04 µm (0.5P-I4). They are ordered in the following order of size: $S_{0.5P\text{-}I4} << S_{0.5P\text{-}I3} < S_{0.5P\text{-}I2} << S_{0.5P\text{-}I1}$. Therefore, in the present experimental conditions, the samples comparison indicates that the microstructure of extruded rods tends to refine with increasing milling intensity. In particular, the relatively small grain size difference between samples 0.5P-I2 and 0.5P-I3 is correlated with a smaller intensity gap between I2 and I3 compared to the rest (qualitatively evaluated as a function of mean milling rotational speed). This influence of milling intensity on grain size in consolidated ODS steel is referenced in literature [35].

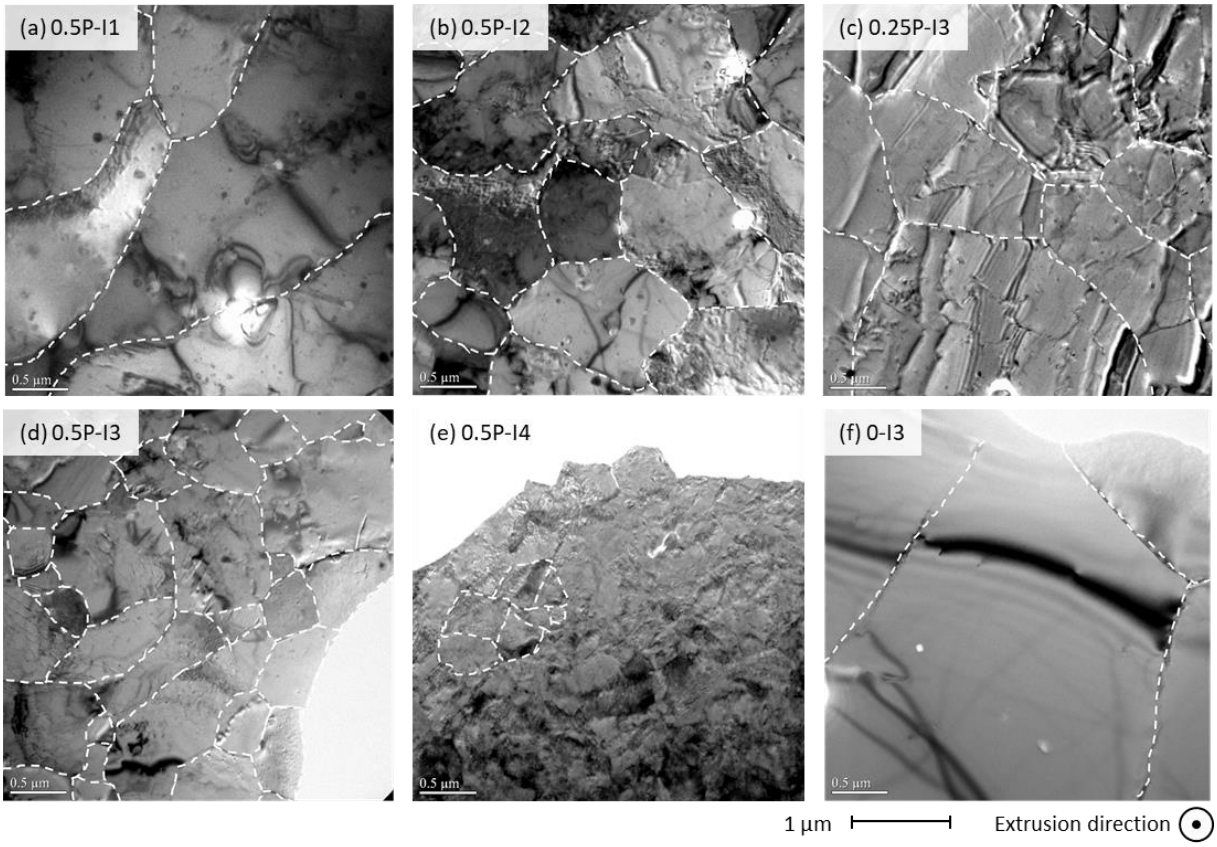

Figure 8: Bright field TEM images at low magnification showing grain size of consolidated materials (a) 0.5P-I1, (b) 0.5P-I2, (c) 0.25P-I3, (d) 0.5P-I3, (e) 0.5P-I4 and (f) 0-I3

	0.5P-I1	***0.5P-I2***	***0.5P-I3***	***0.5P -I4***	***0.25P-I3***	***0-I3***	***0.5CV-I3***
Grain size (µm)	1.23 ± 0.13	0.79 ± 0.07	0.67 ± 0.07	0.33 ± 0.04	1.15 ± 0.17	4.01 ± 0.74	0.76 ± 0.08
Anisotropy factor	1.5	1.6	1.6	1.4	1.5	1.5	1.6

Table 3: Grain size and anisotropy factor measured from TEM images of the extruded steels

Microvickers hardness tests are performed on the extruded materials. Also, prior to extrusion, characterization of the milled powders chemistry, and especially of the oxygen content, is performed. These two parameters are plotted in Figure 9 along with the inverse of grain size, to visualize their evolution with milling intensity. Microhardness Vickers measurements performed on I1, I2, I3, I4 indicate a general rising of hardness with increasing milling intensity. This is correlated both to a global rising of the oxygen content and to a decrease of grain size. It can be noticed that grade 0.5P-I3 displays a slightly lower hardness than 0.5P-I2, which is not in the general evolution way of the test set, and that the oxygen content follows exactly the same tendency. The evolution of hardness of the elaborated steels is then consistent with the evolution of solid solution hardening and grain size contributions.

Additionally, the presence of dislocations could participate to the hardness increase with higher milling intensity. Dislocation density is not evaluated in this work, but it has been demonstrated that the increase of milling intensity entails increased internal stress and hardness of milled powders [36]. This characteristic could be retained after consolidation of the powders.

The contribution of precipitates, however, does not seem to be a preponderant factor for specimens with milling intensities from I2 to I4 at least. Indeed, grades 0.5P-I2, 0.5P-I3

and 0.5P-I4 all show similar features in terms on nanosized precipitates. SAXS measurements indicate a precipitate density of the order of 10^{23} m^{-3} for a mean size of about 2-4 nm, when grade 0.5P-I1 presents a lower precipitates density (in the order of 10^{19} m^{-3}). This grade would therefore be less strengthened by small particles.

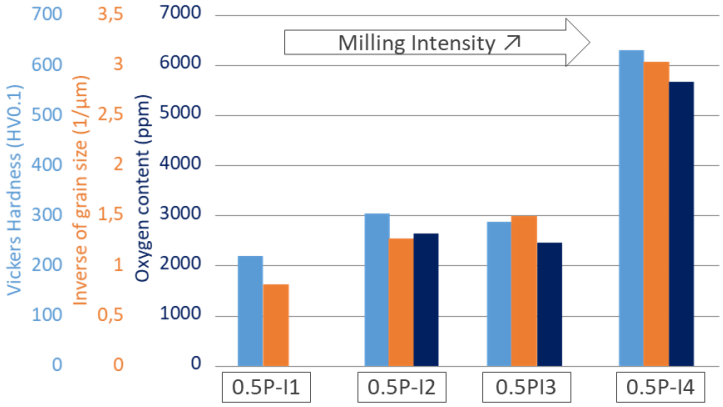

Figure 9: Representation of Vickers hardness, inverse of grain size of extruded materials and oxygen content of the milled powders for grades produced with different milling intensities. The data of O content for sample 0.5P-I1 is not available.

The effect of milling intensity on the chemical and microstructural features of the powders and consolidated material reflects also, in the end, on the mechanical properties. Charpy results (Figure 10) highlight the degradation of impact toughness properties resulting from increased milling intensity. This is particularly visible with grade 0.5P-I4, milled with the highest intensity, which USE reaches only 0.5 J. This phenomenon could be explained by the high reactivity of the milled powder with elements from the atmosphere, increased after high intensity milling. Indeed, high N and C contents in the material can reduce ductility significantly [37], as N tends to segregate along grain boundaries, leading the material to be more brittle. The erosion of the vial, mill and balls can also be the source of contamination.

Due to a lack of material, I1 could not be tested, but from the look of the Vickers hardness results, it seems like this grade would present high performances in tensile strength and poor elongation, and therefore poor impact toughness. This would correlate to previous observations from Kim *et al.*, who showed higher milling intensity induced higher milling efficiency, with a finer and more homogeneous microstructure, but also resulted in higher tensile strength and lower elongation [35].

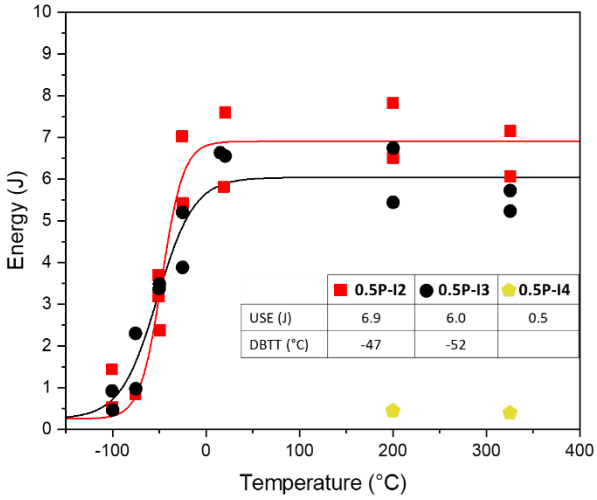

Figure 10: Charpy impact test results of grades elaborated with different milling intensities

c. Influence of the reinforcement rate

To evaluate the influence of reinforcement particles content on the material properties, three grades are produced at I3 milling intensity with different rates of $Y_2Ti_2O_7$ powder: the standard 0.5 wt.% (0.5P-I3), and intermediate 0.25 wt.% (0.25P-I3), and a steel free of reinforcement (0-I3).

The evaluation of the grain size of extruded bars by TEM image analysis (Figure 8 c, d and f and Table 3) shows clearly the influence of the rate of reinforcement on the mean grain size. Grades 0.5P-I3, 0.25P-I3 and 0-I3 display mean grain size of 0.67 ± 0.07 µm, 1.15 ± 0.17 µm and 4.01 ± 0.74 µm, respectively. Therefore, the increase of reinforcement rate induces a refinement of the microstructure, as observed on conventional grades [38]. Indeed, in ODS steels, the nanoparticles restrain the motion of grain boundaries during heat treatments, limiting grain growth [39].

Figure 11 displays the results of Charpy tests on grades produced with different reinforcement rates. Grade 0-I3, free of reinforcement, presents good impact toughness properties, with a USE of 8,2 J and a DBTT of -110°C. With the addition of reinforcement for the two other grades, the DBTT rises and the USE decreases to -52°C and 6.0 J, respectively, for grade 0.5P-I3. This result shows that an increase in reinforcement particles content leads to a significant decrease in impact toughness properties. Grades with less reinforcement display higher USE and lower DBTT. He *et al.* have similar conclusions on ODS conventional grade with various Ti contents [8].

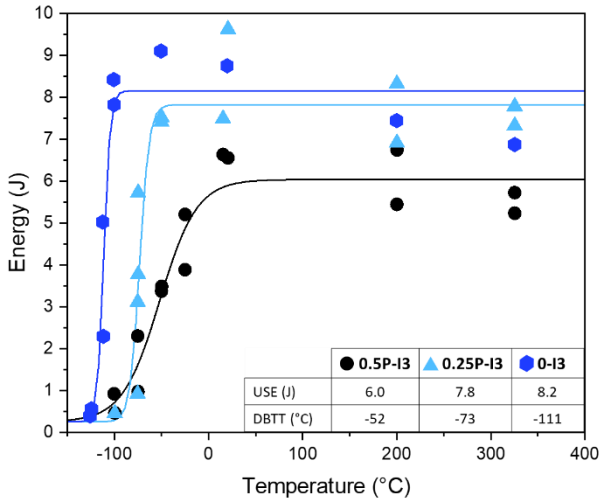

Figure 11: Charpy impact test results of grades elaborated with different reinforcement rates

Concerning tensile properties, Figure 12 shows the evolution of yield strength and total elongation of the three grades elaborated with different reinforcement rates. Grade 0-I3, free of reinforcement, displays rather low strength (253 MPa at 20°C) compared to grade 0.5P-I3 (747 MPa at 20°C). The elongation of grade 0-I3 is also higher, especially at 650°C with 70% total elongation. Grade 0.25P-I3 presents intermediate properties. Therefore, an increased reinforcement rate induces higher strength and lower elongation. The increase in nanoparticles density prevents even more the motion of dislocations, strengthening the material and decreasing ductility. These results are also observed on conventional grades [40].

Therefore, reinforcement rate is crucial for mechanical properties. The introduction of reinforcement particles in metallic matrix induces an increase in tensile strength paired with a decrease in ductility and impact toughness properties.

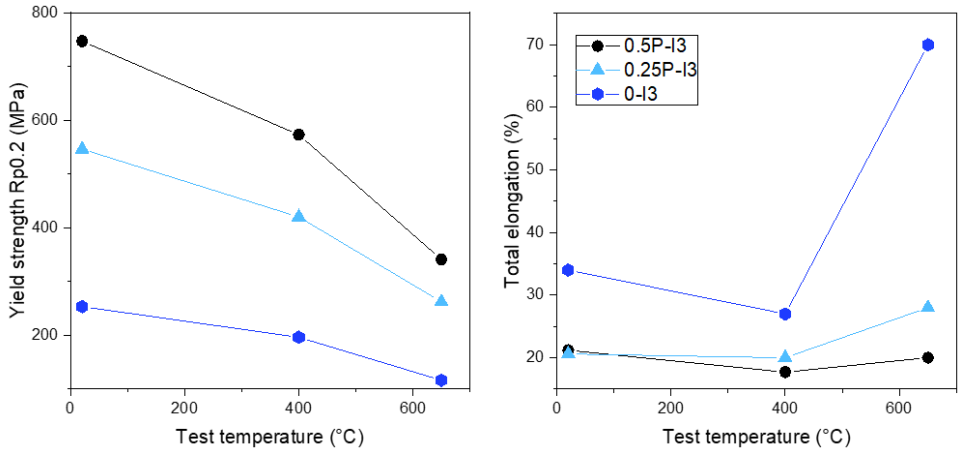

Figure 12: Yield strength and total elongation displayed during tensile tests by grades elaborated with different reinforcement rates: 0.5 wt.% (0.5P-I3), 0.25 wt.% (0.25P-I3) and without introduction of reinforcement particles (0-I3).

Results show that grade 0.25P-I3 seems to be a favorable compromise between grqdes 0.5P-I3 and 0-I3. Indeed, its impact toughness properties are very close to those of the reinforcement-free grade 0-I3, with a USE of 7.8 J, and its tensile properties are closer to those of the reinforced grade 0.5P-I3. The 0.25 wt.% Y_2Ti_2O7 reinforced grade therefore combines good impact properties and good tensile strength. In addition, it appears that 0.25P-I3 has better impact properties than the conventional 0.5CV-I3 grade (Figure 6). Its USE is

higher (7.8 J against 7.4 J) and its DBTT is lower (-73.3°C against -42°C). The 0.5 wt.% reinforcement rate was initially chosen to match the Fe-14Cr-1W-0.3Ti-0.3Y_2O_3 grade, for which the impact properties are the best obtained with the conventional elaboration process [39]. According to the innovative manufacturing range proposed in this study, these results lead to conclude to the necessity to perform an optimization study of the reinforcement rate in order to improve the properties of the material. The optimal reinforcement rate may differ depending on the nature of the introduced elements. The introduction of $Y_2Ti_2O_7$ reinforcements seems to require a smaller amount of mass reinforcement compared to simultaneous introduction of Y_2O_3 and TiO_2 to achieve optimal impact properties.

d. Incorporation mechanism of particles based on TEM investigation

HRTEM analyses performed on the materials from this study show particles with variable size and a structure compatible with Face Centered Cubic (FCC) pyrochlore $Y_2Ti_2O_7$. However, other types of particles are observed in the materials, and in particular, polycristalline particles, as shown in Figure 13 and Figure 14.

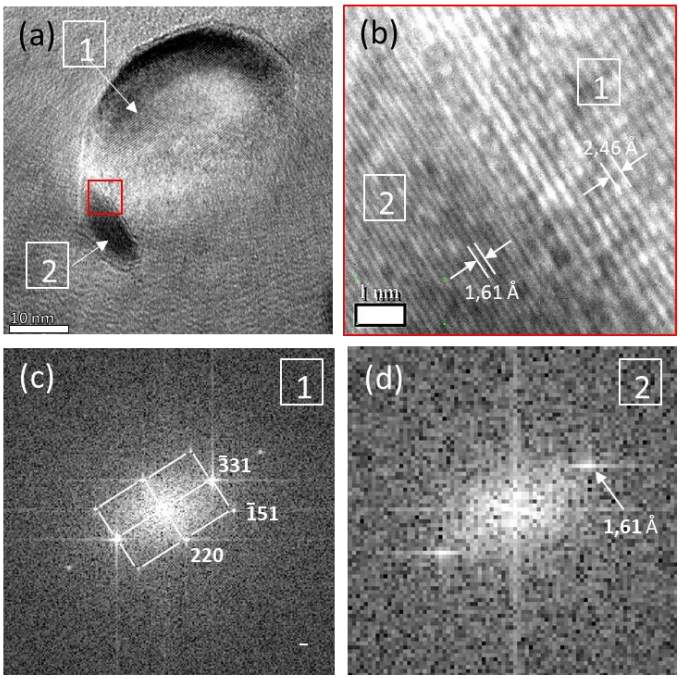

(e)

Area	*hkl*	*Measured Dhkl*	*Theoretical Dhkl*
1	331	2.51	2.32
1	220	3.86	3.57
1	151	2.18	1.94
2	620	1.61	1.60

Figure 13: HRTEM images of a polycristalline particle (a) bright-field picture with two distinct crystalline zones, (b) zoom on the interface between zones 1 and 2, (c) FFT of area 1, (d) FFT of area 2 and (e) table summarizing the measured interplanar distances and matching theoretical interplanar distances of the areas

Figure 13 shows HRTEM images of a large particle (50 nm) presenting two distinct areas (numbered 1 and 2 on the picture). The zoom on the interface (Figure 13.b) shows that both parts have a crystalline structure but different interplanar spacings. Fast Fourier Transformation (FFT) performed on the signal corresponding to area 1 (Figure 13.c) is coherent with a FCC cubic $Y_2Ti_2O_7$ pyrochlore structure in a $[1\bar{1}6]$ axis zone with a calculated lattice parameter of 10.95 Å. For area 2, interplanar measured spacing (Figure

13.d) is in accordance with plans (620) of the pyrochlore structure (no complete FFT could be resolved). Hence, this particle appears to be composed of two distinct pyrochlore crystallites with different orientations.

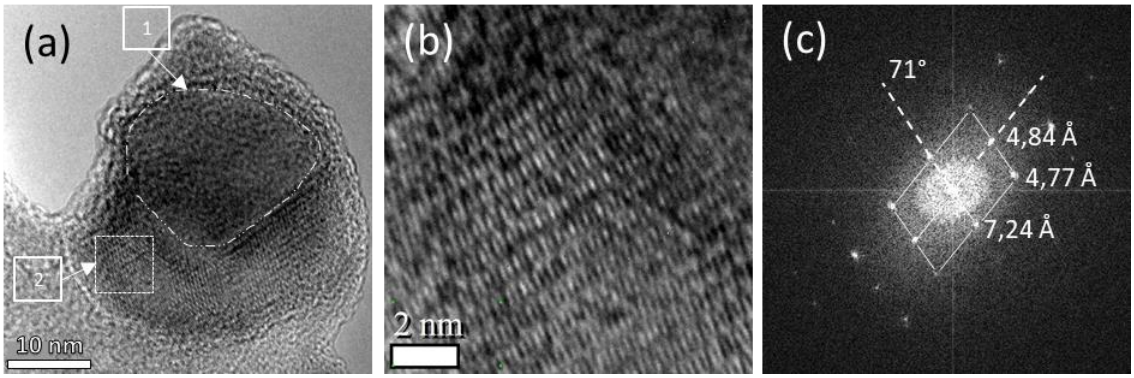

Figure 14: HR-TEM pictures of a "biphased" particle, (a) bright-field image showing to distinct parts of the particle, (b) zoom on part 2 structure, (c) FFT of part 2.

Figure 14 shows another example of a "biphased" particle. In this case, the upper part (zone 1) is a disordered domain (amorphous), which does not exhibit any lattice fringes. The lower part (zone 2) has a crystalline structure (Figure 14.b), and the associated FFT (Figure 14.c) attests of the crystalline structure. This particle, nearly spherical and incoherent with the matrix, is composed of a crystalline domain and an amorphous domain.

Similar "biphased" particles have been observed in the literature. In a Fe-16Cr-4.5Al-0.3Ti-2W-0.37Y_2O_3 ODS steel, Hsiung *et al.* characterized through EFTEM and HRTEM complex-oxide Y-Al-O nanoparticles with a crystalline core and an amorphous shell, or with several crystalline domains [41]. The authors explain this feature by the amorphization of oxide nanoparticles during the MA process of the ODS steel followed by their crystallization during consolidation.

Discussion

These observations lead to the proposition of an introduction mechanism of $Y_2Ti_2O_7$ particles in the metallic matrix. It involves the partial or total amorphization of oxide nanoparticles during the MA of the ODS steel followed by their crystallization during the steel consolidation process. Some particles might undergo, during MA, an only partial amorphization and would be constituted of a crystalline $Y_2Ti_2O_7$ part and of an amorphous part. During the subsequent heat treatment and consolidation, several phenomena can be considered:

- The amorphous part crystallizes with a modified orientation from the already-crystalline part. The after-consolidation particle presents then two differently oriented distinct phases, as shown in Figure 13.
- The amorphous crystalline part remains amorphous, and the after-consolidation particle is biphased with a crystalline part and an amorphous part, as shown in Figure 14.

A second hypothesis would be that the amorphization of the particles takes place during milling, but the recrystallization afterwards would be incomplete. This would explain the unidentified crystalline structure of the particle observed in Figure 14. Indeed, the sharp and angular interface between the both particle areas is probably due to the fragmentation of a powder particle during MA. An amorphous domain stays adjacent to the recrystallized fragment, which is no longer $Y_2Ti_2O_7$ but an unidentified structure. Similar observations are made in the study of Hsiung *et al.*, with an amorphous domain adjacent to a recrystallized

fragment which is no longer Y_2O_3 but $Y_4Al_2O_9$ [41]. This suggests that a solid-state amorphization occurred during the MA, presumably through disordering and solute mixing of initial powder particle fragments with the matrix constituents (Fe, Cr,W).

Then, the results suggest that the introduced $Y_2Ti_2O_7$ powder particles are amorphized during MA and they recrystallize during consolidation. Once the particle is amorphous, crystallization does not necessarily lead to the pyrochlore form, as the chemical composition of the particle might have been altered during amorphization through the introduction of matrix constituents (Fe, Cr, W). The introduction mechanism could then explain the Cr enrichment identified in most particles by EFTEM (Figure 15) and confirmed by EDX measurements. Both techniques reveal that inclusions contained in the powder (before consolidation and after milling) as well as in the densified material are rich not only in Ti, Y and O, but also in Cr. Chromium is included in the particles as soon as right after the milling step. Cr enrichment is often observed in ODS nanoparticles, but mostly is the shape of a shell, with a Y-T-O crystalline core [42], [43]. In the absence of Ti in the composition, Cr has been noticed in Y-Cr-O precipitates [12], [22], [44], revealing that chromium has a strong affinity with oxygen. In particular, a study showed the presence of large Y-Ti-Cr-O oxides in a 14Cr (wt.%) grade elaborated by co-milling of the metallic powder with TiH_2, YH_2 and Fe_2O_3 powders [45].

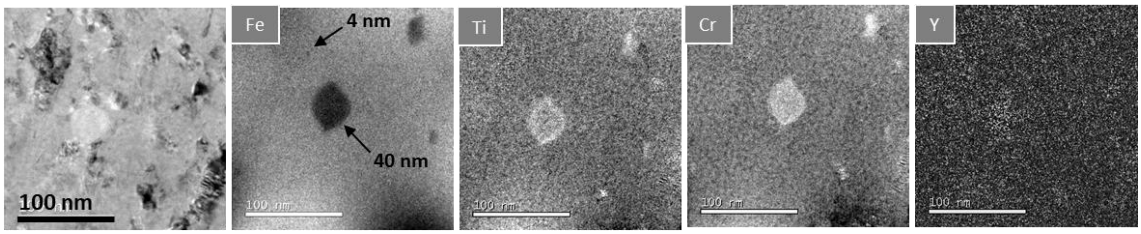

Figure 15: EFTEM analysis of sample 0.5P-I3

Figure 16 proposes a schematic view of the different processes leading to the different types of observed particles in the material. First possibility, the particle is a non-coherent pyrochlore particle. (1) It can originate in the simple fragmentation of the introduced $Y_2Ti_2O_7$ oxide nano-powder during milling, followed by its stabilization during the subsequent heat treatments. Or (2), it can come from the recrystallization of a particle that was amorphised during the milling. (3) An amorphization can also lead to a particle presenting two distinct areas, either both crystalline, or with a remaining amorphous area. Finally (4), small (< 5 nm) coherent pyrochlore particles most probably originate from the nucleation of precipitates from elements issued by the decomposition of the oxide powder during the milling.

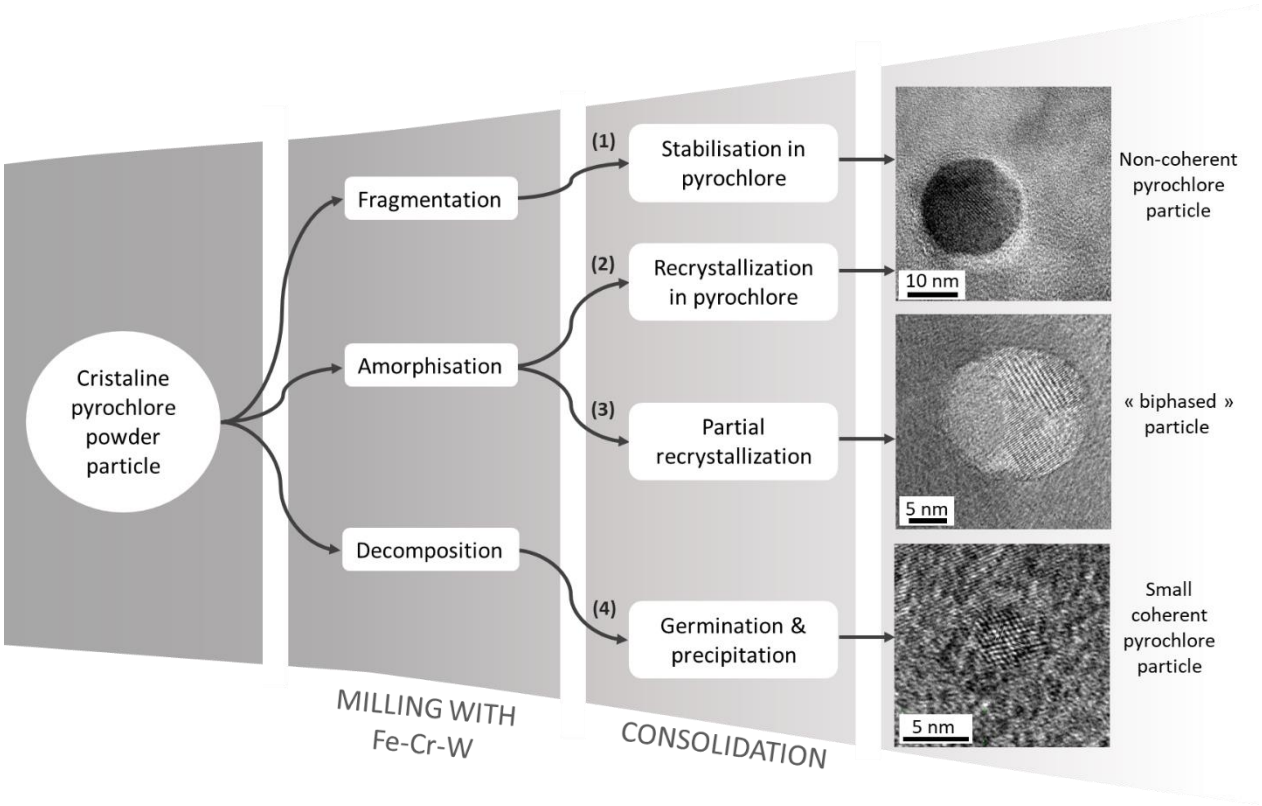

Figure 16 : Schematic representation of the suggested different mechanisms through which particles are incorporated in ODS steels

4. Conclusion

In this paper, an innovative method for ODS production is presented. It involves the introduction of $Y_2Ti_2O_7$ pyrochlore phase as a strengthening powder during the milling. Materials produced with this new process are compared to a conventional material, in all respects similar except for the use of Y_2O_3 + TiO_2 powders as a strengthening powder. These results show that the production of ODS steel with a high density of nanosized precipitates is possible through the introduction of $Y_2Ti_2O_7$ powder as a reinforcement powder. The following conclusions can be drawn:

- The introduction of strengthening elements in the form of $Y_2Ti_2O_7$ pyrochlore, compared to the conventional way, tends to decreasing the number of large (> 100 nm) precipitates.
- No segregation at the grain boundaries is observed in these new materials. This is a particularly interesting feature, considering that in most cases, ODS materials present large oxides (e.g. TiO_2) at grain boundaries, inducing a degradation of the mechanical properties.
- A high density of Y_2Ti_2O nanoparticles, especially for sizes smaller than 5 nm, is contained in the new grades elaborated with the studied method.
- The proposed innovative way, by introducing reinforcement via $Y_2Ti_2O_7$, leads to a more homogeneous material with less coarse precipitates and more reliable impact properties compared to the conventional introduction of Y_2O_3 + TiO_2.

This study also evaluated the influence of different elaboration parameters in this innovative process such as milling intensity and reinforcement rate.

- Low-intensity milling of metal powder and $Y_2Ti_2O_7$ oxide powder leads to a significant heterogeneity by creating aggregates of nanoparticles in the material.
- Very high intensity milling process homogenizes the mixture and produces a material with a fine microstructure, but a drastic decrease in the resilience properties is observed.
- The influence of milling intensity reflects not only on the size of powder particles after the milling, but also has consequences after consolidation: an increased milling intensity induces a finer microstructure in the dense material.
- A reduced milling intensity leads to reduced hardness as well as better impact toughness properties.
- With increased rate of $Y_2Ti_2O_7$, the material shows refined microstructure due to the effect of nanoprecipitates on the motion of grain boundaries during heat-treatments.
- Reinforcement rate is critical on mechanical properties, as an increase rate of $Y_2Ti_2O_7$ induces higher tensile strength, lower ductility and lower impact toughness properties. However, a favorable compromise could be found closer to 0.25 wt.% $Y_2Ti_2O_7$. An additional study would be requested in order to find the amount of $Y_2Ti_2O_7$ optimizing the mechanical properties, and, additionally, more mechanical characterizations will have to be carried out in order to optimize the process

Finally, this study highlights the presence of "biphased" particles comprising either two crystalline parts of different orientation or structure, or a crystalline part and an amorphous part. This lead to propose a mechanism for the introduction of reinforcements. The agglomerated $Y_2Ti_2O_7$ powder particles would be reduced to nanometric sizes and amorphized during grinding. The consolidation would then induce the crystallization of the amorphized particles, according to the pyrochlore $Y_2Ti_2O_7$ structure or other structures that can be linked to the introduction of matrix elements into the particle. The EFTEM analyses showed in particular the recurring presence of chromium in the precipitates.

5. Aknowledgement

The authors would like to thank J.-L. Flament and E. Pons for tensile tests, and P. Wident and R. Le Coz for Charpy tests all from SRMA. The authors also acknowledge Nathalie Boudet, Nils Blanc, Gilbert Chahine and Stephan Arnaud, the scientific team of D2AM-BM02 beamline of the ESRF synchrotron.

6. Data availability

The raw/processed data required to reproduce these findings cannot be shared at this time due to technical or time limitations.

7. References

[1] P. Yvon and F. Carré, "Structural materials challenges for advanced reactor systems," *J. Nucl. Mater.*, vol. 385, no. 2, pp. 217–222, 2009, doi: http://dx.doi.org/10.1016/j.jnucmat.2008.11.026.

[2] A. Alamo, V. Lambard, X. Averty, and M. H. Mathon, "Assessment of ODS-14%Cr ferritic alloy for high temperature applications," *J. Nucl. Mater.*, vol. 329–333, pp. 333–337, 2004, doi: 10.1016/j.jnucmat.2004.05.004.

[3] R. L. Klueh, “Elevated temperature ferritic and martensitic steels and their application to future nuclear reactors,” *Int. Mater. Rev.*, vol. 50, no. 5, pp. 287–310, 2005, doi: 10.1179/174328005X41140.
[4] S. Ukai and M. Fujiwara, “Perspective of ODS alloys application in nuclear environments,” *J. Nucl. Mater.*, vol. 307–311, pp. 749–757, 2002, doi: 10.1016/S0022-3115(02)01043-7.
[5] T. Yamamoto *et al.*, “The transport and fate of helium in nanostructured ferritic alloys at fusion relevant He/dpa ratios and dpa rates,” *J. Nucl. Mater.*, vol. 367–370, pp. 399–410, 2007, doi: 10.1016/j.jnucmat.2007.03.047.
[6] P. D. Edmondson, C. M. Parish, Y. Zhang, A. Hallén, and M. K. Miller, “Helium entrapment in a nanostructured ferritic alloy,” *Scr. Mater.*, vol. 65, no. 8, pp. 731–734, 2011, doi: 10.1016/j.scriptamat.2011.07.024.
[7] M. Klimiankou, R. Lindau, and A. Möslang, “Energy-filtered TEM imaging and EELS study of ODS particles and Argon-filled cavities in ferritic–martensitic steels,” *Micron*, vol. 36, no. 1, pp. 1–8, 2005, doi: 10.1016/j.micron.2004.08.001.
[8] P. He, M. Klimenkov, R. Lindau, and A. Möslang, “Characterization of precipitates in nano structured 14% Cr ODS alloys for fusion application,” *J. Nucl. Mater.*, vol. 428, no. 1–3, pp. 131–138, 2012, doi: 10.1016/j.jnucmat.2011.08.026.
[9] V. de Castro *et al.*, “Mechanical dispersion of Y2O3 nanoparticles in steel EUROFER 97: process and optimisation,” *J. Nucl. Mater.*, vol. 322, no. 2–3, pp. 228–234, 2003, doi: 10.1016/S0022-3115(03)00330-1.
[10] D. T. Hoelzer, J. Bentley, M. A. Sokolov, M. K. Miller, G. R. Odette, and M. J. Alinger, “Influence of particle dispersions on the high-temperature strength of ferritic alloys,” *J. Nucl. Mater.*, vol. 367–370, pp. 166–172, 2007, doi: 10.1016/j.jnucmat.2007.03.151.
[11] A. Ramar, N. Baluc, and R. Schäublin, “On the lattice coherency of oxide particles dispersed in EUROFER97,” *J. Nucl. Mater.*, vol. 386–388, pp. 515–519, 2009, doi: 10.1016/j.jnucmat.2008.12.137.
[12] V. de Castro, E. A. Marquis, S. Lozano-Perez, R. Pareja, and M. L. Jenkins, “Stability of nanoscale secondary phases in an oxide dispersion strengthened Fe–12Cr alloy,” *Acta Mater.*, vol. 59, no. 10, pp. 3927–3936, 2011, doi: 10.1016/j.actamat.2011.03.017.
[13] P. Olier, M. Couvrat, C. Cayron, N. Lochet, and L. Chaffron, “Incidence of mechanical alloying contamination on oxides and carbides formation in ODS ferritic steels,” *J. Nucl. Mater.*, vol. 442, no. 1–3, pp. S106–S111, 2013, doi: 10.1016/j.jnucmat.2013.03.090.
[14] P. Olier *et al.*, “Chemical and microstructural evolution on ODS Fe–14CrWTi steel during manufacturing stages,” *J. Nucl. Mater.*, vol. 428, no. 1–3, pp. 40–46, 2012, doi: 10.1016/j.jnucmat.2011.10.042.
[15] R. L. Klueh, J. P. Shingledecker, R. W. Swindeman, and D. T. Hoelzer, “Oxide dispersion-strengthened steels: A comparison of some commercial and experimental alloys,” *J. Nucl. Mater.*, vol. 341, no. 2–3, pp. 103–114, 2005, doi: 10.1016/j.jnucmat.2005.01.017.
[16] R. Kasada, N. Toda, K. Yutani, H. S. Cho, H. Kishimoto, and A. Kimura, “Pre- and post-deformation microstructures of oxide dispersion strengthened ferritic steels,” *J. Nucl. Mater.*, vol. 367–370, pp. 222–228, 2007, doi: 10.1016/j.jnucmat.2007.03.141.
[17] H. Sakasegawa *et al.*, “Correlation between chemical composition and size of very small oxide particles in the MA957 ODS ferritic alloy,” *J. Nucl. Mater.*, vol. 384, no. 2, pp. 115–118, 2009, doi: 10.1016/j.jnucmat.2008.11.001.
[18] Z. Oksiuta, P. Olier, Y. de Carlan, and N. Baluc, “Development and characterisation of a new ODS ferritic steel for fusion reactor application,” *J. Nucl. Mater.*, vol. 393, no. 1, pp. 114–119, 2009, doi: 10.1016/j.jnucmat.2009.05.013.

[19] X. Boulnat, M. Perez, D. Fabrègue, S. Cazottes, and Y. de Carlan, "Characterization and modeling of oxides precipitation in ferritic steels during fast non-isothermal consolidation," *Acta Mater.*, vol. 107, pp. 390–403, 2016, doi: 10.1016/j.actamat.2016.01.034.
[20] H. Sakasegawa *et al.*, "Microstructural evolution during creep of 9Cr-ODS steels," *Fusion Eng. Des.*, vol. 81, no. 8–14, pp. 1013–1018, 2006, doi: 10.1016/j.fusengdes.2005.09.045.
[21] M. Loyer-Prost, "Influence des conditions de broyage sur la microstructure et les propriétés mécaniques des aciers ODS," Université de Rennes 1, 2014.
[22] M. Dadé, "Plasticité d'alliages nanorenforcés pour le gainage combustible des réacteurs de 4ème génération: compréhension et modélisation de l'influence des différents paramètres microstructuraux sur le comportement d'alliages modèles," Université Grenoble Alpes, 2015.
[23] M. Klimiankou, R. Lindau, and A. Möslang, "Direct correlation between morphology of (Fe,Cr)23C6 precipitates and impact behavior of ODS steels," *Proc. Twelfth Int. Conf. Fusion React. Mater. ICFRM-12*, vol. 367–370, Part A, pp. 173–178, 2007, doi: 10.1016/j.jnucmat.2007.03.150.
[24] A. Steckmeyer *et al.*, "Tensile properties and deformation mechanisms of a 14Cr ODS ferritic steel," *J. Nucl. Mater.*, vol. 405, no. 2, pp. 95–100, 2010, doi: 10.1016/j.jnucmat.2010.07.027.
[25] R. Kasada *et al.*, "Anisotropy in tensile and ductile–brittle transition behavior of ODS ferritic steels," *Proc. ICFRM-14*, vol. 417, no. 1, pp. 180–184, 2011, doi: 10.1016/j.jnucmat.2010.12.069.
[26] T. Liu, L. Wang, C. Wang, H. Shen, and H. Zhang, "Feasibility of using Y2Ti2O7 nanoparticles to fabricate high strength oxide dispersion strengthened Fe–Cr–Al steels," *Mater. Des.*, vol. 88, pp. 862–870, 2015, doi: http://dx.doi.org/10.1016/j.matdes.2015.08.118.
[27] E. Simondon, P.-F. Giroux, L. Chaffron, A. Fitch, P. Castany, and T. Gloriant, "Mechanical synthesis of nanostructured $Y_2Ti_2O_7$ pyrochlore oxides," *Solid State Sci.*, vol. 85, pp. 54–59, 2018, doi: 10.1016/j.solidstatesciences.2018.09.006.
[28] Y. Sakai, K. Tamanoi, and N. Ogura, "Application of tanh curve fit analysis to fracture toughness data of Japanese RPVS," *Nucl. Eng. Des.*, vol. 115, no. 1, pp. 31–39, 1989, doi: 10.1016/0029-5493(89)90257-4.
[29] M. Dadé *et al.*, "Influence of microstructural parameters on the mechanical properties of oxide dispersion strengthened Fe-14Cr steels," *Acta Mater.*, vol. 127, pp. 165–177, 2017, doi: 10.1016/j.actamat.2017.01.026.
[30] T. Okuda and M. Fujiwara, "Dispersion behaviour of oxide particles in mechanically alloyed ODS steel," *J. Mater. Sci. Lett.*, vol. 14, no. 22, pp. 1600–1603, 1995, doi: 10.1007/BF00455428.
[31] A. Deschamps, F. De Geuser, J. Malaplate, and D. Sornin, "When do oxide precipitates form during consolidation of oxide dispersion strengthened steels?," *J. Nucl. Mater.*, vol. 482, pp. 83–87, 2016, doi: 10.1016/j.jnucmat.2016.10.017.
[32] M. J. Alinger, G. R. Odette, and D. T. Hoelzer, "On the role of alloy composition and processing parameters in nanocluster formation and dispersion strengthening in nanostuctured ferritic alloys," *Acta Mater.*, vol. 57, no. 2, pp. 392–406, 2009, doi: 10.1016/j.actamat.2008.09.025.
[33] G. Spartacus *et al.*, "Nano-oxide precipitation kinetics during the consolidation process of a ferritic oxide dispersion strengthened steel.," *Scr. Mater.*, vol. 188, pp. 10–15, Nov. 2020, doi: 10.1016/j.scriptamat.2020.07.003.

[34] A. García-Junceda, M. Hernández-Mayoral, and M. Serrano, “Influence of the microstructure on the tensile and impact properties of a 14Cr ODS steel bar,” *Mater. Sci. Eng. A*, vol. 556, pp. 696–703, 2012, doi: 10.1016/j.msea.2012.07.051.
[35] J.-H. Kim *et al.*, “Effects of processing condition on the microstructural and tensile properties of 14Cr-based oxide dispersion strengthened alloys,” *J. Nucl. Mater.*, vol. 449, no. 1–3, pp. 300–307, 2014, doi: 10.1016/j.jnucmat.2013.09.043.
[36] A. Pandey, K. Jayasankar, P. Parida, M. Debata, B. K. Mishra, and S. Saroja, “Optimization of milling parameters, processing and characterization of nano-crystalline oxide dispersion strengthened ferritic steel,” *Powder Technol.*, vol. 262, pp. 162–169, 2014, doi: 10.1016/j.powtec.2014.04.070.
[37] J. H. Kim *et al.*, “Cryomilling effect on the mechanical alloying behaviour of ferritic oxide dispersion strengthened powder with Y_2O_3,” *J. Alloys Compd.*, vol. 580, pp. 125–130, 2013, doi: 10.1016/j.jallcom.2013.04.165.
[38] B. Hary, “Compréhension et modélisation de l’influence du taux de renforts et de la texture de déformation sur la recristallisation des aciers ODS ferritiques,” 2017.
[39] M. Couvrat, “Fabrication d’aciers ODS à haute performance : relation procédé - microstructure - propriétés mécaniques,” Université de Rennes 1, 2013.
[40] M. Praud, “Plasticité d’alliages renforcés par nano-précipitation,” Université de Toulouse, 2012.
[41] L. L. Hsiung *et al.*, “Formation mechanism and the role of nanoparticles in Fe-Cr ODS steels developed for radiation tolerance,” *Phys. Rev. B*, vol. 82, no. 18, 2010, doi: 10.1103/PhysRevB.82.184103.
[42] A. J. London *et al.*, “Effect of Ti and Cr on dispersion, structure and composition of oxide nano-particles in model ODS alloys,” *Acta Mater.*, vol. 97, pp. 223–233, 2015, doi: 10.1016/j.actamat.2015.06.032.
[43] E. Marquis, “Core/shell structures of oxygen-rich nanofeatures in oxide-dispersion strengthened Fe–Cr alloys,” *Appl. Phys. Lett.*, vol. 93, no. 181904, 2008, doi: 10.1063/1.3000965.
[44] P. He, “On the structure-property correlation and the evolution of Nanofeatures in 12–13.5% Cr oxide dispersion strengthened ferritic steels,” Karlsruhe Institute of Technology, 2012.
[45] Y. Wen *et al.*, “Innovative processing of high-strength and low-cost ferritic steels strengthened by Y–Ti–O nanoclusters,” *Mater. Sci. Eng. A*, vol. 544, pp. 59–69, 2012, doi: 10.1016/j.msea.2012.03.015.

Declaration of interests

☒ The authors declare that they have no known competing financial interests or personal relationships that could have appeared to influence the work reported in this paper.

☐The authors declare the following financial interests/personal relationships which may be considered as potential competing interests:

Highlights

- ODS steels were produced using an innovative manufacturing process where $Y_2Ti_2O_7$ pyrochlore oxide nanoparticles are introduced directly into the Fe-Cr metallic powder through mechanical milling.
- This innovative method is efficient to obtain competitive ODS steels with a more homogeneous microstructure, less coarse precipitates and more reliable impact properties compared to the conventional process.
- The study also underlines the influence of milling intensity and reinforcement rate on microstructural and mechanical properties of the consolidated material.
- This study highlights the presence of “biphased” particles comprising either two crystalline parts of different orientation or structure, or a crystalline part and an amorphous part.